Streamlined QPS Control With Magnetizing Current Injection for All-ZVS Operation in Decoupled-Type Triple Active Bridge Converters

Linxiao Gong, *Graduate Student Member, IEEE*, Yunfeng Peng, Junzhong Xu, *Member, IEEE*, Wenhui Li, Xing Fang, *Student Member, IEEE*, Jian Wang, and Yong Wang, *Member, IEEE*

***Abstract*—The decoupled-type triple active bridge converter (DTAB) offers improved power density and power-decoupling features by removing an auxiliary inductance from one port. However, traditional phase-shift modulation schemes fail to extend the zero-voltage-switching (ZVS) range, limiting efficiency and practical application. To broaden the ZVS range of DTAB converters, in this paper, a streamlined quadruple phase-shift (QPS) modulation scheme, evolved form the volt–sec-balance principle in dual active bridge (DAB) converters, is proposed to achieve ZVS operation in the two ports maintained with the auxiliary inductance. To avoid increasing computational burden, the influence of magnetizing inductance is considered for the ZVS operation in the inductance-canceled port, whose optimal design is analyzed, particularly suitable for DTAB converters. Consequently, this software–hardware-integrated strategy offers computational efficiency, particularly advantageous for time-intensive scenarios such as electric vehicle (EV) charging system. Additionally, to simplify the ZVS analysis, a unified ZVS model of DTAB converters based on the complete circuit response equation is introduced, obviating the need for complex mode-dependent ZVS analysis and also applicable to TAB converters. Finally, the efficacy of the proposed strategy is validated in a 3.3 kW/100 kHz SiC-based DTAB prototype, tailored to the EV a plications, achieving peak efficiency of 95% at partial load conditions.**

***Index Terms*—Decoupled-type triple active bridge (DTAB) converters, magnetizing inductance, quadruple phase-shift (QPS) modulation scheme, rms current, zero-voltage-switching (ZVS) range optimization.**

I. INTRODUCTION

BENEFITING from the low manufacturing cost, high-power density, centralized control advantages, multiport converters have recently attracted great research attention as a prominent strategy for the renewable energy industry [1], [2], [3]. As one of the representative topologies within the multiwinding transformer-coupled multiport converters family, the triple active bridge (TAB) converter, consisting of a three-port transformer and three full-bridge modules, has found extensive adoption in the electric vehicles (EVs) charging system [4], [5], dc microgrid, uninterrupted power supplies.

Since the introduction of the TAB converter, scholarly research has predominantly focused on addressing power-decoupling and efficient operation issues. For power-decoupling, a substantial body of research involving both software and hardware levels has been successively reported. At the software level, a prevalent research approach involves simplifying the cross-coupled multiinput-multioutput system into several independent single-input-single-output control loops by matrix transformation [6], [7], [8]. However, the effectiveness of software decoupling is closely associated with the phase-shift dimension, and significant performance reductions occur when a higher dimension phase-shift control scheme is adopted. Furthermore, complex matrix transformations are required in the computation of decoupling coefficients, diminishing the practicality of software strategies.

At the hardware decoupling level, a primary approach entails constructing a zero-impedance loop to clamp the magnetic flux variation of the transformer with a stiff voltage source. The authors in [9], [10], [11], and [12] introduced an *LC* resonant network into TAB converters and specified the switching frequency to the resonant point for achieving power-decoupling operation. However, the additional capacitive components could increase the power loss and degrade the high-power-density advantage of TAB converters. In Hazra et al.'s [13] work, a cost-effective decoupling method is proposed, where the auxiliary inductance at one port is directly removed to clamp the magnetic flux variation. The system topology after removal of the inductance is illustrated in Fig. 1, which consists of a full-bridge port without auxiliary inductance (master port) and two full-bridge ports with retained auxiliary inductance (slave port). In such a configuration, power decoupling can be achieved without any

Manuscript received 2 February 2024; revised 13 May 2024; accepted 22 June 2024. Date of publication 9 July 2024; date of current version 4 September 2024. This work was supported by the China Postdoctoral Science Foundation under Grant 2022M722057. Recommended for publication by Associate Editor Yam Siwakoti. *(Corresponding author: Yunfeng Peng.)*

Linxiao Gong, Junzhong Xu, Wenhui Li, Xing Fang, and Yong Wang are with the Key Laboratory of Control of Power Transmission and Conversion of Ministry of Education, Shanghai Jiao Tong University, Shanghai 200240, China, and also with the Department of Electrical Engineering, Shanghai Jiao Tong University, Shanghai 200240, China (e-mail: gonglx@sjtu.edu.cn; junzhongxu@sjtu.edu.cn; GGLeelwhui@sjtu.edu.cn; xing_fang@sjtu.edu.cn; wangyong75@sjtu.edu.cn).

Yunfeng Peng is with the Department of Automation, Shanghai Jiao Tong University, Shanghai 200240, China, and also with the Key Laboratory of System Control and Information Processing, Ministry of Education of China, Shanghai 200240, China (e-mail: pengyf@sjtu.edu.cn).

Jian Wang is with the College of Smart Energy, Shanghai Jiao Tong University, Shanghai 200240, China (e-mail: wj1071268395@sjtu.edu.cn).

Color versions of one or more figures in this article are available at https://doi.org/10.1109/TPEL.2024.3424850.

Digital Object Identifier 10.1109/TPEL.2024.3424850

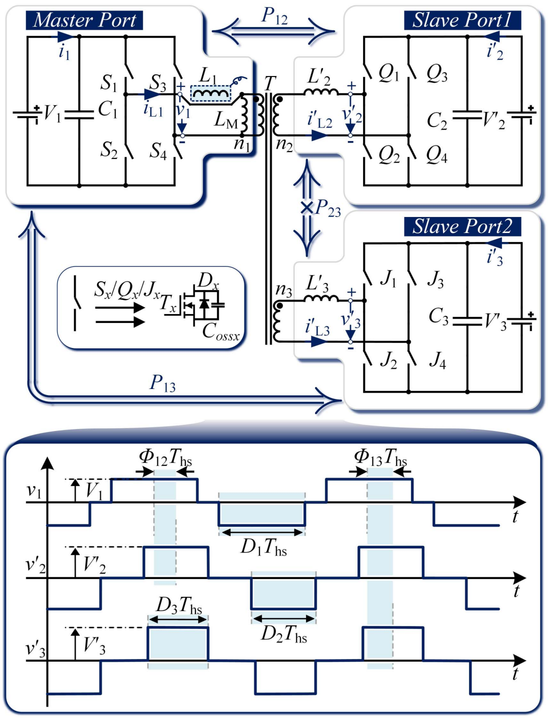

Fig. 1. Circuit schematic of the DTAB converter and the definition of phase-shift angles in this article.

software or hardware measures, enhancing the power-density of TAB converters further. Furthermore, characterized by its power decoupling characteristics, the converter can be decomposed into two independent dual active bridge (DAB) converters for analysis [14], providing significant convenience for the phase-shift modulation (PSM) design. In the subsequent discussion, such a TAB converter with the inductance-canceled configuration is referred to the decoupled-type triple active bridge (DTAB) converter, whose operating mechanism and decoupling characteristics have been thoroughly investigated and verified in [13], [14], and [15]. Nevertheless, the power transmissions in the aforementioned studies [13], [14], and [15] are all based on low-dimensional phase-shift control schemes, resulting in a significantly restricted zero-voltage-switching (ZVS) range for DTAB converters, particularly under voltage-mismatch conditions. In pursuit of high power-density, DTAB converts are usually designed to operate at a relatively high-frequency switching condition, where the switching-ON loss becomes nonnegligible due to the narrowed ZVS range, significantly degrading the operational efficiency and compromising the applicability of DTAB converters. Therefore, it is essential to realize the wide ZVS-range operation of DTAB converters.

Regarding the ZVS operation mechanism, due to the intricate mode classification of the phase-shift control, most ZVS analyses for TAB converters are mode-dependent and nonunified [16], [17], [18]. For example, in [16] and [17], the ZVS process of TAB converters is divided into four or six intervals in a two-port view. Li et al. [18] further simplified the ZVS process into three intervals according to the symmetry of the TAB operation. Although the ZVS modes of the TAB converters are appropriately classified in [16], [17], and [18], the complex mode classification introduces challenges in formulating wide ZVS-range control schemes. Moreover, the dead-time effect is not considered in the above-mentioned studies. The inconsistent configuration of dead-time and resonance time can result in failed ZVS operation.

For the PSM scheme with wide ZVS-range, the majority of research is conducted by combining Fourier transform theory within the frequency domain. In Dey et al.'s [17] work, a power loss model for TAB converters is established to optimize the ZVS range of the system. However, the obtained phase-shift results are prestored in the chip and applied in the form of a lookup table. In Li et al.'s [18] work, a particle swarm optimization algorithm is employed to optimize both the ZVS range and the rms current, with phase-shifting trajectory data precalculated through an algorithmic iteration process. In summary, optimal control in [17] and [18] can only be implemented through lookup tables or online fitting, and efficiency reductions are observed when the hardware parameters change. Furthermore, the presence of multiorder functions in the frequency domain greatly complicates system analysis, making it challenging to obtain an explicit mathematical expression for optimal phase-shift control, thereby degrading the applicability of control schemes. On the contrary, based on time-domain analysis, mathematical trajectories of phase-shift control can be derived, enabling the realization of real-time calculation. Michon et al. [19] first applied the single-phase shift (SPS) control in DAB converters to the TAB converter. Although this control scheme is straightforward, it results in high turn-off currents and backflow power under voltage mismatch conditions, leading to low operational efficiency. Building upon the widely adopted volt–second balance (VSB) control [a simplified extended phase-shift (EPS) control] from DAB converters [20], [21], [22], the authors of [23] and [24], respectively, introduced the VSB control into the TAB converters and modular multiactive bridge (MMAB) converters, revealing a simplified control system, superior conduction losses, and a relatively expanded ZVS range characteristic characteristics. However, the influence of the switches' body-capacitance and the dead time on the ZVS operation is overlooked in [23] and [24], which constrains the ZVS range and poses challenges to achieve the all-ZVS operation. On the hardware level, authors of [21] and [25] incorporated a well-tuned magnetizing inductance into DAB converters, validating the feasibility of the magnetizing inductance in expanding the ZVS range and simplifying the design of PSM schemes. Furthermore, Gong et al. [26] considered the optimal design of magnetizing inductance in TAB converters, effectively expanding the ZVS range of TAB converters. However, due to the differing equivalent topologies of DTAB and TAB converters, the optimal design methodology of magnetizing inductance in Gong et al.'s [28] work is not suitable for the all-ZVS operation in DTAB converters.

In conclusion, to achieve efficient and low computational operation of the DTAB converter, this article first analyzes the ZVS operation mechanism of the DTAB converter, and a unified ZVS analysis model is proposed by combining the complete response circuit equations. Building upon this unified model, this article further introduces a straightforward software–hardware-integrated approach for DTAB converters to realize full-range

ZVS operation. In the software level, a simplified quadruple phase-shift (QPS) modulation scheme is developed for the ZVS operation of the slave ports' switches. This scheme introduces phase-shift compensation into the VSB control, and considers the impact of switches' body capacitance and dead time in the ZVS process. On the hardware side, the influence of magnetizing inductance is considered in this article, whose optimal design customized for DTAB converters is also discussed in detail. The main contributions of this article can be summarized as follows.

1) Proposal of a unified ZVS model for the DTAB converter, eliminating the need for intricate ZVS mode classification and simplifying the design of the wide-ZVS-range phase-shift control schemes, which are also applicable to TAB converters.
2) Introduction of a hybrid software–hardware approach with all-ZVS operation characteristic. This approach combines a simplified QPS modulation scheme, evolved from the VSB control in the DAB converter, with a well-tuned magnetizing inductance, expanding the ZVS range of the DTAB converter to the entire spectrum of voltage and load conditions.
3) All analyses are grounded in the time-domain model of the DAB converter. The all-ZVS operation strategy is computationally stress-free and can be readily realized in real-time control without any lookup tables or online iteration, particularly suitable for the computation-intensive EVs charging system.

The rest of this article is organized as follows. In Section II, the power-decoupling characteristic of the DTAB converter is analyzed, and the basic operational principle of VSB control in the DAB perspective is explained. In Section III, a comprehensive analysis of the unified ZVS model is performed and all ZVS operation conditions are derived under the VSB control. In Section IV, the hybrid software–hardware all-ZVS operation strategy is proposed and analyzed. In Section V, the control loop design of the hybrid scheme, the theoretical ZVS range, and the rms current characteristic are analyzed and compared in detail. Experiment results are given in Section VI. Finally, Section VII concludes this article.

II. OPERATION OF DTAB CONVERTER UNDER THE VSB CONTROL SCHEME

A. DTAB Converter and the Power-Decoupling Feature

The circuit schematic of the DTAB converter is shown in Fig. 1, where the inductance L_1 is canceled. The V_1, V_2', and V_3' represent three dc voltage sources, with paralleled connected filter capacitances C_1, C_2', and C_3'. The labels of switches in three ports are divided into S_x, Q_x, and J_x, where $x = 1, 2, 3, 4$. The simplified model of the switches $S_x/Q_x/J_x$ is composed of transistor T_x, antiparallel diode D_x, and equivalent drain-to-source body-capacitance $C_{\mathrm{oss}x}$. The inductances L_1, L_2', and L_3' are defined as the unit lump sum of the external series inductance and the leakage inductance of the transformer. The three full bridges are coupled by a three-winding transformer T, whose turns ratios are defined as n_1, n_2, and n_3, and L_{M} is the transformer's magnetizing inductance. Furthermore, the i_1, i_2', and i_3' represent the output current of each port. i_{L1}, i_{L2}', and i_{L3}' are defined as the current flowing through the inductances. The v_1, v_1', and v_3' are the midpoint voltage of each full active bridge. The phase-shift angles in this article are defined in Fig. 1, where D_{x} represents the duty ratio of the middle voltage v_{x} and $D_{\mathrm{x}} = [0, 1], x = 1, 2, 3$. T_{hs} is defined as half of the switching period. In addition, variables Φ_{12}, Φ_{13} are the relative phase-shift angles of v_1 to the center axis of v_2 and v_3, and $\Phi_{1\mathrm{x}} = [-0.5, 0.5], x = 2, 3$.

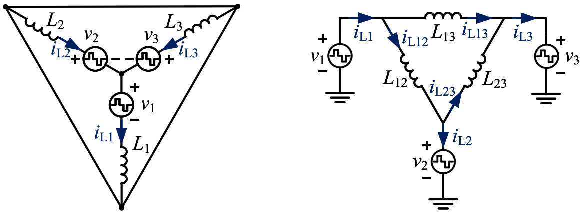

(a) (b)

Fig. 2. Equivalent circuits of TAB converters. (a) Y-type circuit. (b) Δ-type circuit.

Generally, the TAB converter can be equivalently transformed into Y-type and Δ type circuits according to the classical equivalent transformation of the multiport circuit, as depicted in Fig. 2(a) and 2(b).

To simplify the analysis, the electrical variables in Fig. 2 can be expressed as follows:

$$\begin{cases} L_2 = n_{12}^2 L_2'; i_{\mathrm{L2}} = n_{12} i_{\mathrm{L2}}^{'}; v_2 = v_2^{'}/n_{12} \\ L_3 = n_{13}^2 L_3'; i_{\mathrm{L3}} = n_{13} i_{\mathrm{L3}}^{'}; v_3 = v_3^{'}/n_{13} \\ L_{12} = L_1 + L_2 + L_1 L_2/L_3 \\ L_{13} = L_1 + L_3 + L_1 L_3/L_2 \\ L_{23} = L_2 + L_3 + L_2 L_3/L_1 \end{cases} \tag{2}$$

where $n_{12} = n_2/n_1, n_{13} = n_3/n_1$, and $n_{23} = n_3/n_2$. According to Fig. 2(b), the transmitted power of each port can be decomposed into two parts, as expressed in the following:

$$P_1 = P_{12} + P_{13}, P_2 = P_{12} - P_{23}, P_3 = P_{13} + P_{23}$$

where the P_{xy} represents the coupled power transmitted from port x to port y, which can be calculated by (1) shown at the bottom of this page [27].

Therefore, When P_1 is required to be changed, both the subcomponents P_{12} and P_{13} would undergo variations. However,

---

$$P_{\mathrm{xy}} = \frac{4}{f_{\mathrm{s}}\pi^3} \sum_{k=1}^{2m+1} \frac{1}{k^3} \left\{ \frac{V_{\mathrm{x}} V_{\mathrm{y}} \cos\left[\frac{k\pi}{2}(1 - D_{\mathrm{x}})\right] \cos\left[\frac{k\pi}{2}(1 - D_{\mathrm{y}})\right] \sin\left[k\pi \Phi_{\mathrm{xy}}\right]}{L_{\mathrm{xy}}} \right\}, x \neq y \neq z \in [1, 2, 3]. \tag{1}$$

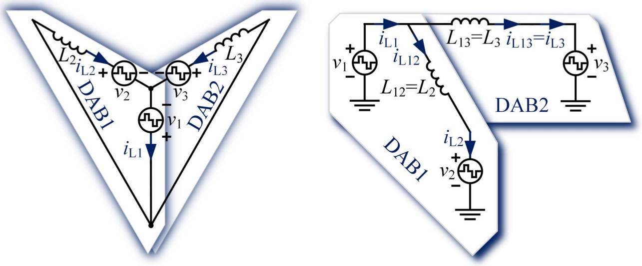

(a) (b)

Fig. 3. Equivalent circuits of DTAB converters. (a) Y-type circuit. (b) Δ-type circuit.

P_{12} and P_{13} are integral parts of P_2 and P_3, leading to power coupling issues in the other two ports.

Fig. 3(a) and 3(b) illustrates the two-type equivalent circuits of the DTAB converter. After canceling the inductance L_1, it becomes evident that the inductance currents at ports 2 and 3 are entirely determined by v_1 and corresponding middle point voltage source. Based on (1), it can be inferred that if $L_1 \approx 0$, i.e., $L_{12} \to \infty$ and $L_{23} \to \infty$, P_{12} and P_{13} would approximate zero. Consequently, the power transfer of the DTAB converter can be expressed as follows:

$$P_1 = P_{12} + P_{13}, P_2 = P_{12}, P_3 = P_{13}$$

i.e., coupled terms P_{12} and P_{13} are mitigated in P_3 and P_2. Therefore, the power-decoupled operation can be achieved in the DTAB converter without any software or hardware measures, whose basic operating mechanism and power-decoupling characteristics have been thoroughly validated in [13], [14], and [15].

It is worth noting that the removal of the auxiliary inductance from port 1 determines that the voltage variation of v_1 would influence the operation of the other two ports. Therefore, port 1 can be referred to as the master port. The power transmission of the other two ports is governed by the master port and referred to as the slave port. According to Fig. 3, the inductance currents of each port can be expressed as follows:

$$\begin{cases} i_{\mathrm{L1}}(t) = i_{\mathrm{L12}}(t) + i_{\mathrm{L13}}(t) \\ i_{\mathrm{L2}}(t) = i_{\mathrm{L12}}(t) \\ i_{\mathrm{L3}}(t) = i_{\mathrm{L13}}(t). \end{cases} \tag{3}$$

Therefore, the DTAB converter can be considered as the superposition of two DAB converters operating simultaneously, allowing system analysis to be conducted from the perspective of a single DAB converter. Given the complete symmetry of the two slave ports, the subsequent research will concentrate on the master port and slave port 1.

B. Volt–Sec Balance Control in DAB Converters

PSM is the primary control method for power transmission in both DAB and TAB converters. The voltage-second balance control, i.e., a simplified EPS control, has garnered significant attention and application in DAB converters [20], [21], [22], which can be expressed as follows:.

$$V_1 D_1 = V_2 D_2 = V_{\min} \tag{4}$$

where $V_{\min} = \min\{V_1, V_2\}$. This control strategy has been proven featuring superior conduction losses, low current stress, and a relatively expanded ZVS range characteristics, leading to garnered attentions and applications not only in DAB converters but also in TAB converters [23], [26] and MMAB converters [24]. Due to the operational symmetry of the DAB converter, only the buck condition operation of the VSB control is presented here, which can be divided into six patterns, as shown in Fig. 4. Here, t_{Sx} and t_{Qx} represent the turn-ON instants of the switch S_{x} and Q_{x}, respectively. The expressions for all switching currents in each pattern are summarized in Table I, where $K_{21} = V_2/V_1$.

According to Table I and the current conditions (3), the current variations of three ports under VSB control can be drawn, as depicted in Fig. 5. Here, I_{z} represents the per unified current required for the ZVS operation, the optimal calculation of which is detailed in Section III. As observed, after integrating the VSB control into DTAB converters, the magnitudes of all switching currents are less than $|I_{\mathrm{Z}}|$ in most power ranges, meaning that all-ZVS operation cannot be achieved. Therefore, integrating the VSB control into DTAB converters, the switching-ON losses of the DTAB converter cannot be completely eliminated, which degrades operational efficiency especially under high-frequency conditions.

III. UNIFIED ZVS ANALYSIS AND THE DERIVATION OF OPTIMAL ZVS OPERATION CONDITIONS

A. Unified ZVS Analysis of DTAB Converters

To expand the ZVS range of DTAB converters, it is necessary to analyze the ZVS process comprehensively. According to the Thevenin theorem, the DTAB converter can be transformed into a two-port converter [18]. The equivalent converter viewed in port 1 is shown in Fig. 6, where the equivalent inductance L_{eq} and voltage V_{eq} can be expressed as follows:

$$\begin{cases} L_{\mathrm{eq}} = L_1 + L_2 // L_3 // L_{\mathrm{M}} \\ V_{\mathrm{eqt}} = \dfrac{v_2 L_3 L_{\mathrm{M}} + v_3 L_2 L_{\mathrm{M}}}{L_2 L_3 + L_2 L_{\mathrm{M}} + L_3 L_{\mathrm{M}}}. \end{cases} \tag{5}$$

Based on the combination of the switching sequence, the ZVS process can be separately divided into six intervals [16], four intervals [17], and three intervals [18]. Herein, the three intervals are shown in Fig. 6 for the subsequent ZVS analysis.

The realization of ZVS operation is closely related to the dynamic variation of inductance current in dead time, which is mode-dependent and expression-complicated in [16], [17], and [18]. In general, as depicted in Fig. 6, the inductance would exchange energy with various output capacitances of switches at different intervals. For L_{eq} and V_{eqt}, all components of the dashed line can be replaced by an equivalent capacitance C_{eq} with a different initial voltage state $v_{\mathrm{eqc}}(0^+)$. Therefore, the current variation at all intervals can be analyzed in a uniform, full response, second-order equivalent circuit.

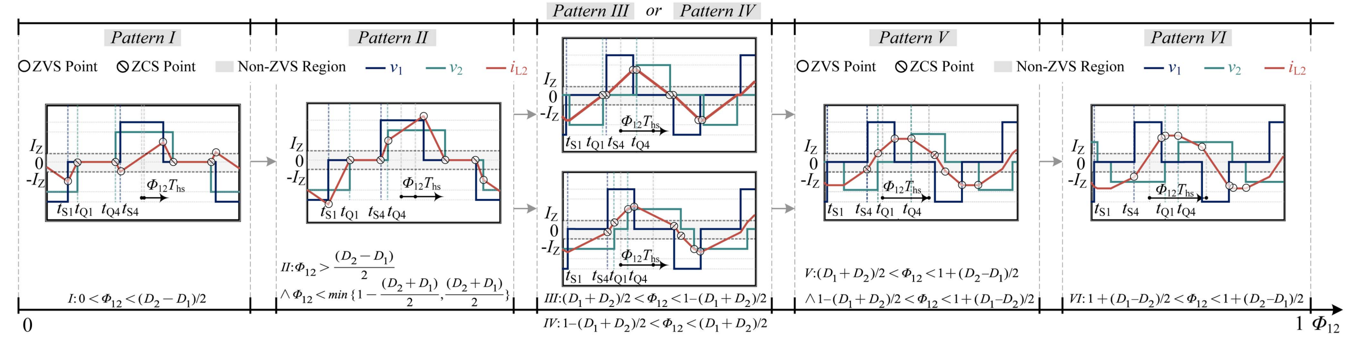

Fig. 4. Pattern classification of the VSB scheme under the buck condition.

TABLE I
TURNING-ON CURRENT AND THE SIMPLIFIED ZVS CONDITION OF ALL SWITCHES IN EACH PATTERN

Pattern	$I(t_{S1})$	$I(t_{S4})$	$I(t_{Q1})$	$I(t_{Q4})$
I	$(K_{21}-1)D_1-2K_{21}\Phi_{12}$	$(K_{21}-1)D_1+2K_{21}\Phi_{12}$	$-D_1+D_2K_{21}$	$-D_1+D_2K_{21}$
II	$(K_{21}-1)D_1-2K_{21}\Phi_{12}$	$-D_1+D_2K_{21}$	$-D_1+D_2K_{21}$	$(K_{21}-1)D_2+2\Phi_{12}$
III	$-D_1-D_2K_{21}$	$-D_1+D_2K_{21}$	$-D_1+D_2K_{21}$	$D_1+D_2K_{21}$
IV	$(K_{21}-1)D_1-2K_{21}\Phi_{12}$	$-(K_{21}+1)D_1+2K_{21}(1-\Phi_{12})$	$(K_{21}+1)D_2-2(1-\Phi_{12})$	$(K_{21}-1)D_2+2\Phi_{12}$
V	$-D_1-D_2K_{21}$	$-(K_{21}+1)D_1+2K_{21}(1-\Phi_{12})$	$(K_{21}+1)D_2-2(1-\Phi_{12})$	$D_1+D_2K_{21}$
VI	$-(K_{21}+1)D_1-2K_{21}(1-\Phi_{12})$	$-(K_{21}+1)D_1+2K_{21}(1-\Phi_{12})$	$D_1+D_2K_{21}$	$D_1+D_2K_{21}$
ZVS Condition	$\leq -I_Z \leq 0$	$\leq -I_Z \leq 0$	$\geq I_Z \geq 0$	$\geq I_Z \geq 0$

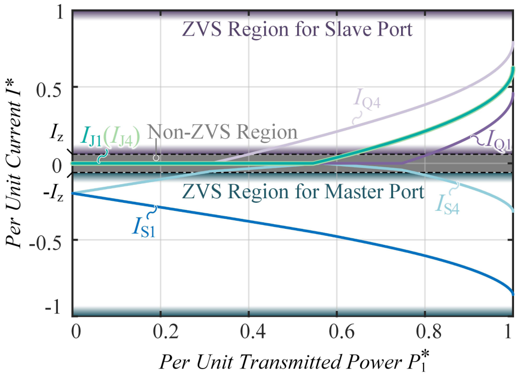

Fig. 5. Turning-ON current of all switches under the VSB scheme with the $L_2 = L_3 = 10\,\mu$H, $C_{\text{oss1}} = C_{\text{oss2}} = C_{\text{oss3}} = 2$ nF, $f_s = 100$ kHz, $V_1 = 160$ V, $V_2 = 120$ V, $V_3 = 100$ V, $P_{12} = P_{13}$.

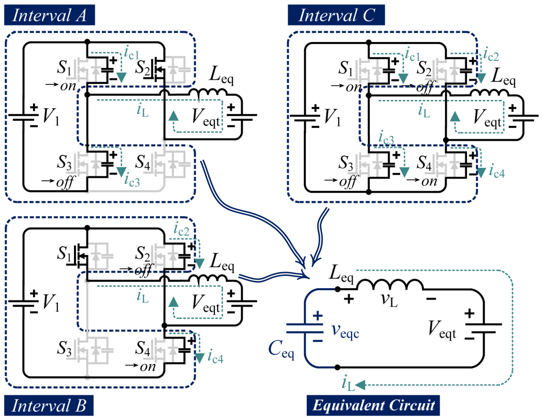

Fig. 6. ZVS modes classification and the unified ZVS model. (Single-switch interval A: S_2, S_3 to S_1, S_2; Single-switch interval B: S_1, S_2 to S_1, S_4; Dual-switches interval C: S_2, S_3 to S_1, S_4.)

Since the inductance current varies sinusoidally in the ZVS process, the following expression can be assumed:

$$i_L(t) = A_1 \sin(\omega t) + A_2 \cos(\omega t)$$

where A_1 and A_2 are constant terms, the ω represents the resonant frequency and $\omega = 1/\sqrt{L_{\text{eq}} C_{\text{eq}}}$. Combined with the initial state conditions

$$i_L\left(0^+\right) = I_{L0}, v_L\left(0^+\right) = v_{\text{eqc}}(0^+) - V_{\text{eqt}} = V_{L0} \tag{6}$$

where I_{L0} and V_{L0} represent the initial state of inductance current and voltage, respectively. The unified expression of $i_L(t)$ and $v_L(t)$ in the resonant process can easily be calculated as follows:

$$\begin{bmatrix} i_L(t) \\ v_L(t) \end{bmatrix} = \begin{bmatrix} V_{L0}/(\omega L_{\text{eq}}) & I_{L0} \\ -I_{L0}\omega L_{\text{eq}} & V_{L0} \end{bmatrix} \begin{bmatrix} \sin(\omega t) \\ \cos(\omega t) \end{bmatrix}. \tag{7}$$

Herein, another state parameter, V_{LE} is introduced to represent the inductance voltage at the end of the resonant process. The ZVS process concludes when the following equation is satisfied:

$$v_L(t) = -I_{L0}\omega L_{\text{eq}} \sin(\omega t) + V_{L0}\cos(\omega t) = V_{LE}.$$

Since the ZVS operation is accompanied by inductance current flowing back to the power source through the antiparallel diode, additional back-flow power would be generated. Hence,

TABLE II
EQUIVALENT PARAMETERS IN THE ZVS PROCESS

interval	V_{L0}	V_{LE}	C_{eq}
A	$-V_1 - V_{\mathrm{eqt}}$	$-V_{\mathrm{eqt}}$	$2C_{\mathrm{oss}}$
B	$-V_{\mathrm{eqt}}$	$V_1 - V_{\mathrm{eqt}}$	$2C_{\mathrm{oss}}$
C	$-V_1 - V_{\mathrm{eqt}}$	$V_1 - V_{\mathrm{eqt}}$	C_{oss}

the current I_{L0} cannot be excessively large and should be sufficient to complete the resonant process. Therefore, the ZVS current I_{Z}, i.e., the minimum current I_{L0} for the ZVS realization, and the corresponding resonant time T_{R} can be solved as follows:

$$\begin{cases} I_{\mathrm{Z}} = I_{\mathrm{L0}} = \begin{cases} -\sqrt{(V_{\mathrm{LE}}^2 - V_{\mathrm{L0}}^2)}/(\omega L_{\mathrm{eq}}), |V_{\mathrm{LE}}| > |V_{\mathrm{L0}}| \\ 0, |V_{\mathrm{LE}}| < |V_{\mathrm{L0}}| \end{cases} \\ T_{\mathrm{R}} = \begin{cases} \dfrac{1}{\omega}\left(\dfrac{\pi}{2} - \arctan\left(\dfrac{V_{\mathrm{L0}}}{\sqrt{V_{\mathrm{LE}}^2 - V_{\mathrm{L0}}^2}}\right)\right), |V_{\mathrm{LE}}| > |V_{\mathrm{L0}}| \\ \dfrac{1}{\omega}\left(\dfrac{\pi}{2} + \arcsin\left(\dfrac{V_{\mathrm{LE}}}{|V_{\mathrm{L0}}|}\right)\right), |V_{\mathrm{LE}}| < |V_{\mathrm{L0}}| \end{cases} \end{cases} \tag{8}$$

where the V_{L0}, C_{eq}, and V_{LE} can be calculated by Table II. It is noteworthy that the unified expressions of $i_{\mathrm{L}}(t)$, $v_{\mathrm{L}}(t)$, I_{Z}, and T_{R} are in complete agreement with those mode-dependent results presented in [16], [17], and [18].

As observed in (8), the current required for ZVS operation I_{Z} is highly correlated with the voltage V_{L0} and V_{LE}. Therefore, to expand the ZVS range of the DTAB converter, the derivation of I_{Z} should be closely in conjunction with the modal characteristics of VSB control.

B. ZVS Condition Derivation Under the VSB Scheme Considering the Dead-Time Effect

Taking the slave port switch Q_1 as an example, the normalized switching-ON current of Q_1 can be uniformly expressed as follows:

$$\begin{aligned} I\left(t_{\mathrm{Q1}}\right) &= \frac{1}{2L_{\mathrm{eq}}I_{\mathrm{N}}}\int_{t_{\mathrm{Q1}}}^{t_{\mathrm{Q1}}+T_{\mathrm{hs}}}\left[v_2(t) - v_1(t)\right]dt \\ &= \frac{1}{2L_{\mathrm{eq}}I_{\mathrm{N}}}\left[-\int_{t_{\mathrm{Q1}}}^{t_{\mathrm{Q1}}+T_{\mathrm{hs}}} v_1(t)dt + D_2V_2T_{\mathrm{hs}}\right] \end{aligned} \tag{9}$$

where $I_{\mathrm{N}} = V_1/(4f_{\mathrm{s}}L_{\mathrm{eq}})$. According to Fig. 4, v_2 always lags behind v_1 and the following expression is obtained:

$$\int_{t_{\mathrm{Q1}}}^{t_{\mathrm{Q1}}+T_{\mathrm{hs}}} v_1(t)dt \leq D_1V_1T_{\mathrm{hs}}$$

i.e.,

$$I\left(t_{\mathrm{Q1}}\right) \geq -D_1 + D_2K_{21}. \tag{10}$$

Substituting (4) into the above-mentioned equation, the relation $I(t_{\mathrm{Q1}}) \geq 0$ can be derived. Similar analysis can be applied to other switching currents, leading to the following conclusions:

$$\begin{cases} \max\left\{I\left(t_{\mathrm{S1}}\right), I\left(t_{\mathrm{S4}}\right)\right\} = -D_1 + D_2K_{21} = 0 \\ \min\left\{I\left(t_{\mathrm{Q1}}\right), I\left(t_{\mathrm{Q4}}\right)\right\} = -D_1 + D_2K_{21} = 0. \end{cases}$$

TABLE III
ZVS PARAMETERS OF THE SWITCHES WITH THE ZCS OPERATION

Pattern	interval	V_{L0}	V_{LE}	Current I_{Z}	Dead Time T_{R}
$S_{4\_\mathrm{II,III}}$	B	0	V_1	$V_1\sqrt{\dfrac{2C_{\mathrm{oss1}}}{L_{\mathrm{eq1}}}}$	$\pi\sqrt{\dfrac{L_{\mathrm{eq1}}C_{\mathrm{oss1}}}{2}}$
$Q_{1\_\mathrm{I,II,III}}$	A	V_2	0	0	$\pi\sqrt{\dfrac{L_2C_{\mathrm{oss2}}}{2}}$
Q_{1_I}, D_2=1	C	-V_2	V_2	0	$\pi\sqrt{L_2C_{\mathrm{oss2}}}$
Q_{4_I}	B	0	-V_2	$V_2\sqrt{\dfrac{2C_{\mathrm{oss2}}}{L_2}}$	$\pi\sqrt{\dfrac{L_2C_{\mathrm{oss2}}}{2}}$

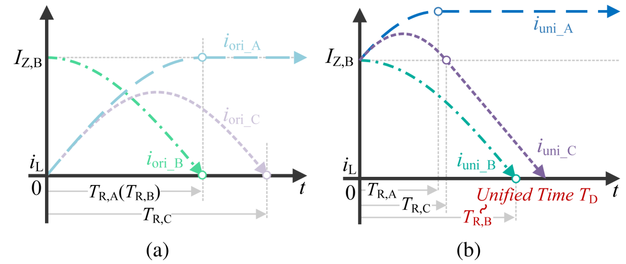

Fig. 7. i_{L} change variation of all intervals in dead time. (a) Change with different ZVS currents I_{z}. (b) Change with unified $I_{\mathrm{Z,B}}$.

However, to ensure the all-ZVS operation of DTAB converters, the following conditions must be satisfied:

$$\begin{cases} \max\left\{I\left(t_{\mathrm{S1}}\right), I\left(t_{\mathrm{S4}}\right)\right\} = -D_1 + D_2K_{21} \leq -I_{\mathrm{z}} \\ \min\left\{I\left(t_{\mathrm{Q1}}\right), I\left(t_{\mathrm{Q4}}\right)\right\} = -D_1 + D_2K_{21} \geq I_{\mathrm{z}}. \end{cases} \tag{11}$$

Therefore, the zero switching current has the maximum deviation from the magnitude $|I_{\mathrm{z}}|$. Once the ZVS operation of such ZCS-operating switches is realized, the all-ZVS operation can be achieved. Table III summarizes the operation modes and electrical parameters of all ZCS-operating switches, wherein $S_{\mathrm{x,y}}$ and $Q_{\mathrm{x,y}}$ represent the ZCS operation of the switch S_{x} or Q_{x} in pattern y. L_{eq1} denotes the equivalent inductance reflected on the primary side from ports 2 and 3, and $L_{\mathrm{eq1}} = L_2//L_3$.

As can be seen, the ZVS current I_{Z} and the required resonant time T_{R} differ among various ZCS patterns. Fig. 7(a) depicts the variations trends with various inductance currents in three intervals, where $T_{\mathrm{R,A}}$, $T_{\mathrm{R,B}}$, and $T_{\mathrm{R,C}}$ represent the resonant time in each interval and $I_{\mathrm{Z,B}}$ denotes the ZVS current of interval B. As observed, the ZVS operation of interval B would fail if the dead time is larger than $T_{\mathrm{R,B}}$ since the current would reverse during a long dead time. Furthermore, the resonant process of interval C cannot be finished if the dead time is configured to $T_{\mathrm{R,B}}$ with a zero initial current.

Therefore, it is imperative to configure the dead time to ensure that each resonant process can be adequately completed, and the inductance current would not reverse at the end of the dead time. Moreover, since the required ZVS current varies with ZCS patterns, it is necessary to uniformly set the ZVS current to maintain the continuity of mode transitions [28].

To guarantee the ZVS operation in any interval, the ZVS current and dead time of slave port 1 can be unified expressed as follows: $I_{\mathrm{Z}} = V_2\sqrt{2C_{\mathrm{oss2}}/L_2}$ and $T_{\mathrm{D}} = \pi\sqrt{L_2C_{\mathrm{oss2}}/2}$, by which the variation trend of inductance current at the three intervals can be drawn in Fig. 7(b). As observed, the resonant process remains unchanged in interval B. With an increased ZVS current I_Z, the resonant process in interval A and C is completed more quickly, resulting in $T_{\mathrm{R,A}}$ and $T_{\mathrm{R,C}}$ being decreased and less than $T_{\mathrm{R,B}}$. Therefore, through this standardized configuration, the resonant process of all intervals can be completed, and the inductance current would not reverse at the end of the dead time. Consequently, the ZVS current and the dead time of all ports can be uniformly set as follows:

$$\begin{cases} I_{\mathrm{Z1}} = V_1\sqrt{2C_{\mathrm{oss1}}/L_{\mathrm{eq1}}} \\ I_{\mathrm{Z2}} = V_2\sqrt{2C_{\mathrm{oss2}}/L_2} \\ I_{\mathrm{Z3}} = V_3\sqrt{2C_{\mathrm{oss3}}/L_3} \\ T_{\mathrm{D}x} = \pi\sqrt{L_{\mathrm{x}}C_{\mathrm{ossx}}/2}, x = 1, 2, 3. \end{cases} \tag{12}$$

Although the above-mentioned analysis is performed under buck condition, the ZVS process of the DTAB converter remains unchanged under different voltage level. Therefore, the ZVS condition of all voltage levels can still be uniformly expressed by (12). Next, based on the above-mentioned ZVS conditions, this article will further design the PSM scheme to extend the ZVS range.

IV. PROPOSED HYBRID ALL-ZVS OPERATION SCHEME

A. Phase-Shift Compensation Design

According to (11) and (12), the ZVS condition of the two slave ports can be reformulated as follows:

$$\begin{cases} -D_1 + D_2K_{21} \geq 4f_{\mathrm{s}}K_{21}\sqrt{2L_2C_{\mathrm{oss2}}}, \text{Slave Port2} \\ -D_1 + D_3K_{31} \geq 4f_{\mathrm{s}}K_{31}\sqrt{2L_3C_{\mathrm{oss3}}}, \text{Slave Port3.} \end{cases} \tag{13}$$

Therefore, the ZVS operation of the two slave ports can be guaranteed with the following relation:

$$\begin{cases} D_1 = \dfrac{V_{\min}}{V_1} - D_{\mathrm{c}} \\ D_{\mathrm{c}} = 4f_{\mathrm{s}} \cdot \max\left\{K_{21}\sqrt{2L_2C_{\mathrm{oss2}}}, K_{31}\sqrt{2L_3C_{\mathrm{oss3}}}\right\}. \end{cases} \tag{14}$$

Fig. 8 illustrates the trend of variation of all switching currents after phase-shift compensation. As can be seen, the turn-on currents of all ZCS-operating switches in the slave ports are elevated to the ZVS region, and the ZVS operation for slave ports is achieved. However, according to (11), the ZVS conditions for the master port and slave port are opposite. Therefore, the switching currents of master port's switches are still situated in the non-ZVS region, indicating that the ZVS operation of master port cannot be realized only by modulating the phase-shift angles.

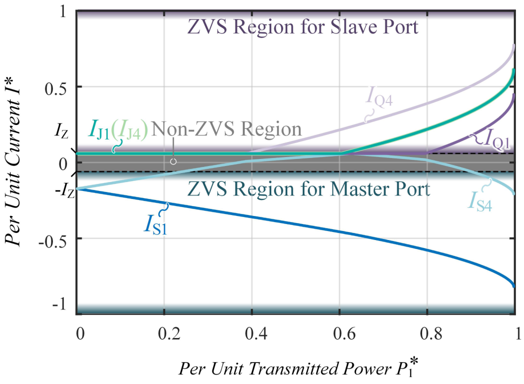

Fig. 8. Variation trend of all switches' turning-ON currents with the phase-shift compensation.

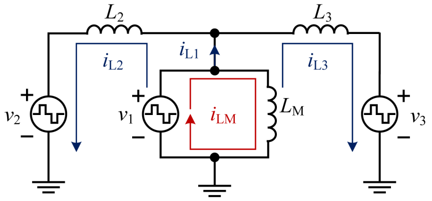

Fig. 9. Equivalent circuit of DTAB converters considering the magnetizing inductance.

B. Determination of the Optimal Magnetizing Inductance

In TAB converters, the magnetizing inductance is typically configured to a value much larger than the auxiliary inductance. Therefore, the influence of the magnetizing inductance on the stable operation of the circuit is usually omitted. In LLC converters, the ZVS operation of the switches primarily relies on the inductive magnetizing current, meaning that it is possible to introduce the optimal design of the magnetizing inductance in DTAB converters to assist in the implementation of ZVS operation. The simplified topology of the DTAB converter considering magnetizing inductance is shown in Fig. 9.

As observed, with the elimination of the auxiliary inductance in the master port, the magnetizing inductance will be completely clamped by the voltage source v_1. This configuration ensures that the magnetizing current i_{LM} flows exclusively into the master port, with no impact on the operation of other slave ports. Consequently, the magnetizing current can be computed as follows:

$$I_{\mathrm{LM}} = \frac{-V_1D_1}{4f_{\mathrm{s}}L_{\mathrm{M}}}. \tag{16}$$

After the phase-shift compensation, the ZVS condition of the master port's switches can be rewritten as follows:

$$I_{\mathrm{LM}} + I_{\mathrm{SC}} \leq -I_{\mathrm{Z1}} \tag{17}$$

$$L_{\mathrm{M}} = \frac{V_{\min}/4f_{\mathrm{s}} - \max\left\{V_{\max,2}\sqrt{2L_2C_{\mathrm{oss2}}}, V_{\max,3}\sqrt{2L_3C_{\mathrm{oss3}}}\right\}}{V_{\max,1}\sqrt{2C_{\mathrm{oss1}}/L_{\mathrm{eq1}}} + 2\cdot\max\left\{V_{\max,2}\sqrt{2C_{\mathrm{oss2}}/L_2}, V_{\max,3}\sqrt{2C_{\mathrm{oss3}}/L_3}\right\}}. \tag{15}$$

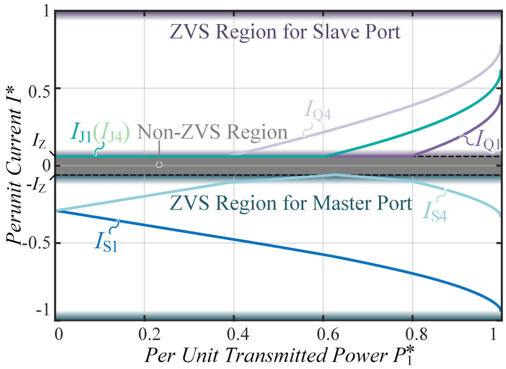

Fig. 10. Current variation with the designed magnetizing inductance.

where the I_{SC} represents the superposition current resulting from the phase-shift compensation and can be expressed as follows:

$$\begin{aligned} I_{SC} &= I_N[(-D_1+K_{21}D_2)+(-D_1+K_{31}D_3)] \\ &= \max\left\{V_2\sqrt{2C_{oss2}/L_2}, V_3\sqrt{2C_{oss3}/L_3}\right\}. \end{aligned} \quad (18)$$

Combining the (12), (16), and (18), the optimal value of the magnetizing inductance can be obtained, as shown in (15) shown at the bottom of previous page. Here, $V_{min} = \min\{V_{min1}, V_{min2}, V_{min3}\}$, and $V_{max,x}$ represent the maximum of V_x. While the provided expression may seem intricate, the computation of L_M is a one-time operation only if the operating parameters of the system are determined. Therefore, the calculation of L_M would not add additional computational burden to the control system.

Fig. 10 illustrates the turning-ON current variations for all switches considering the injection of magnetizing current. As observed, the currents of the master port switches are elevated in the ZVS region, facilitating the all-ZVS operation throughout the entire load range.

Furthermore, Fig. 11 compares the key waveforms of the VSB control, the VSB control with designed magnetizing inductance [26] and the hybrid strategy proposed in this article.

As shown in Fig. 11(a), in the ports 2 and 3, the ZVS operation is only realized in the switches turning on at the peak current. In the port 1, only ZCS operation is realized in all switches, since the switching currents in port 1 can be regarded as the superposition of i_{L2} and i_{L3}. When the VSB control and the hardware design of magnetizing inductance in Gong et al.'s [26] work is adopted in DTAB converters, as shown in Fig. 11(b), ZVS operation ranges are extended but only applicable to master port's switches, since the magnetizing inductance is clamped by voltage source v_1, resulting in the magnetizing current flowing exclusively into port 1, as depicted in Fig. 9. Therefore, the optimization approach proposed in Gong et al.'s [26] work is not suitable for DTAB converters. As shown in Fig. 11(c), the ZVS operation is achieved in all switches of ports 2 and 3 with the phase-shift compensation D_c. Therefore, combined with the magnetizing inductance design for DTAB converters, all-ZVS operation can be achieved. In summary, to realize the ZVS operation of switches in slave ports, a simplified QPS modulation scheme is proposed and shown as follows:

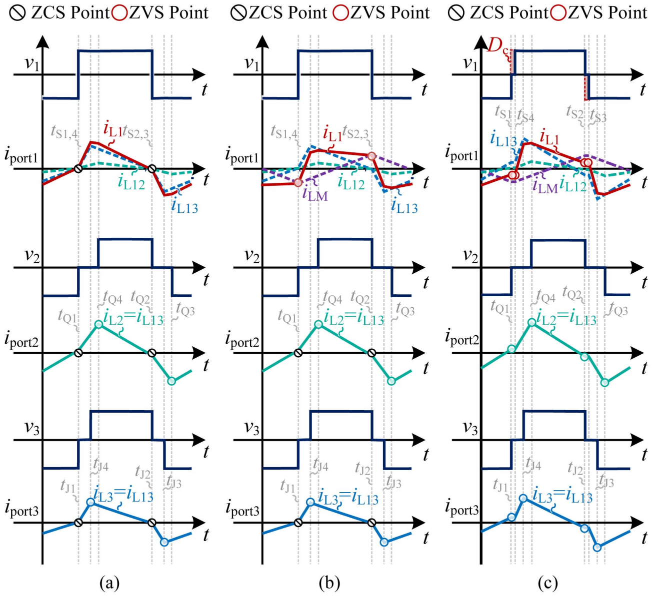

(a) (b) (c)

Fig. 11. Decomposition of the DTAB converter's inductance current. (a) Based on the VSB scheme. (b) Based on the VSB scheme and magnetizing inductance design [26]. (c) Based on the phase-shift compensation and the designed magnetizing inductance.

$$\begin{cases} D_1 = V_{min}/V_1 - D_c \\ D_2 = V_{min}/V_2, D_3 = V_{min}/V_3 \\ D_c = 4f_s \cdot \max\left\{K_{21}\sqrt{2L_2C_{oss2}}, K_{31}\sqrt{2L_3C_{oss3}}\right\}. \end{cases} \quad (19)$$

Notably, since all slave ports in DTAB converters are fully equivalent and symmetric, the proposed control law (19) and the design of magnetizing inductance (15) can be extended to the converters with a port number greater than 3. In the subsequent analysis, this hybrid software–hardware all-ZVS strategy is referred to as the proposed control scheme with the designed magnetizing inductance (PCSL), whose control loop design and operational characteristics will be presented next.

V. ANALYSIS OF THE SYSTEM CHARACTERISTICS

A. DTAB Control Loop

The control loop of the PCSL scheme is illustrated in Fig. 13. Given that ports 2 and 3 are both connected to batteries in the EVs charging system, a dual voltage–current loop configuration is employed here, and the outputs of the proportional–integral loop are set to Φ_{12} and Φ_{13}. Furthermore, in addition to the all-ZVS operation characteristic of the PCSL scheme, the calculation of $\boldsymbol{D} = \{D_1, D_2, D_3\}$ is totally determined by (19) with little computational burden. This streamlined setup is particularly well-suited for computation-intensive EVs charging scenarios, offering advantages over lookup table methods [18] or online iterative control approaches [27], which are complicated and can be sensitive to hardware parameters.

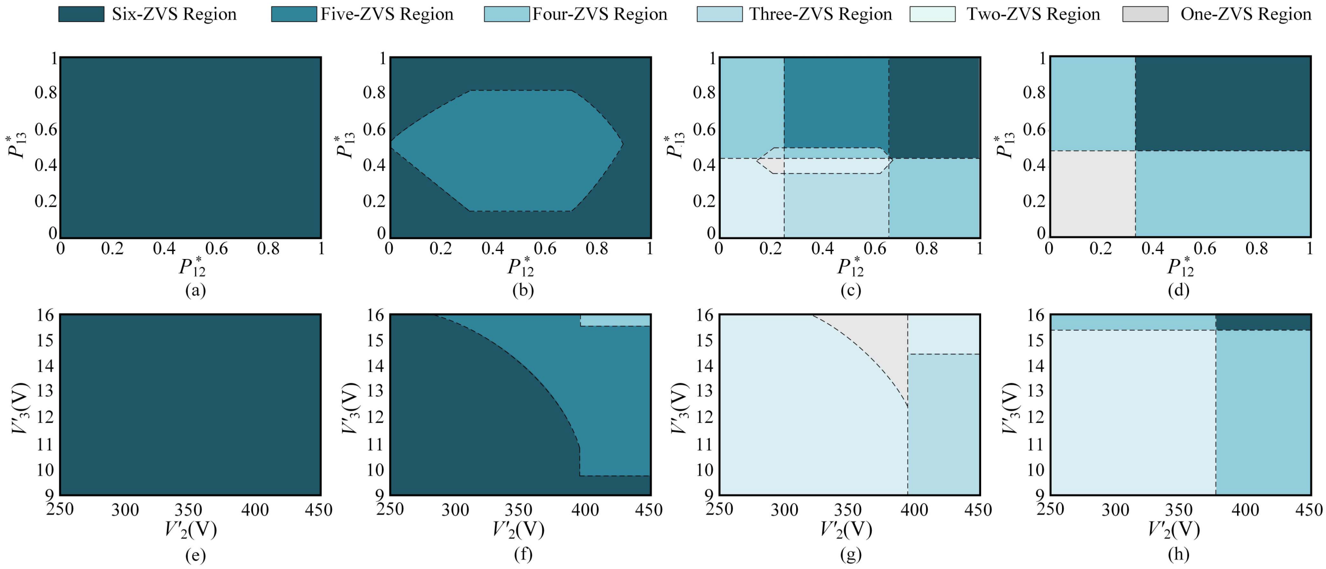

Fig. 12. Comparisons of ZVS operation range. (a) PCSL scheme under the CV condition. (b) PCS scheme under the CV condition. (c) VSB scheme under the CV condition. (d) PSM scheme under the CV condition. (e) PCSL scheme under the CP condition. (f) PCS scheme under the CP condition. (g) VSB scheme under the CP condition. (h) PSM scheme under the CP condition.

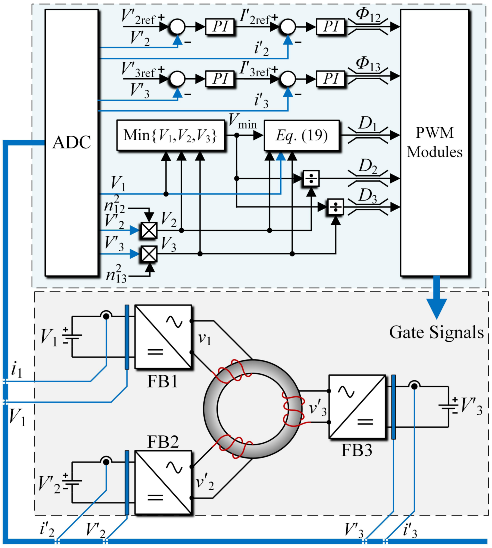

Fig. 13. Control diagram of the proposed control scheme.

B. ZVS Range Comparisons

Fig. 12 compares the theoretical ZVS range among the PCSL scheme, the proposed control scheme without the designed magnetizing inductance (PCS), VSB scheme [23], [26], and the simplest PSM scheme [19] (corresponds to the SPS control in DAB converters). Fig. 12(a)–(d) showcases the ZVS range under the constant voltage (CV) condition with $V_1 = 396$ V, $V_2' = 336$ V, $V_3' = 12$ V. Fig. 12(e) and (f) illustrates the the ZVS range under the constant power (CP) condition with $P_2^* = 0.15, P_3^* = 0.15$, whose operation parameters are identical to those in Table IV. Here, the x-ZVS region represents that there are x bridge arms performing the ZVS operation in this region.

TABLE IV
DESIGN SPECIFICATIONS OF THE TESTING SETUP

Items	Specifications
Operation settings	BUS port: V_1:396V HV port: V_2:250-450V, $P_{2\max}$:3.3kW LV port: V_3:9V-14V, $P_{3\max}$:1kW
S_{1-4} and Q_{1-4}	IV1Q06040T4, TO247-4, $C_{\text{oss}1,2}$ = 470pF
Driver	Si82390AD, $R_{\text{gon}} = R_{\text{goff}}$ = 5Ω
J_{1-4}	NCE30H15, TO-220-3L, $C_{\text{oss}3}$ = 20nF
Driver	Ucc27201A, $R_{\text{gon}} = R_{\text{goff}}$ = 10Ω
Controller	STM32G474RET6 with 6 channels of HRTIMER
Dead Times	$T_{\text{d}1}$:200ns, $T_{\text{d}2}$:200ns, $T_{\text{d}3}$:350ns
Frequency	f_{s} = 100kHz
Inductor L_2'	Inductance: 8μH Litz wire: 6 turns, 0.1mm*800 strands (2.1mΩ) Core: PQ3225, Material: DMR95 (DMEGC)
Inductors L_{31}' and L_{32}'	Inductance: 115nH Copper wire:3 turns, 2mm*5mm, Φ=15mm (0.06mΩ) Core: S3216EQ-E10.3-60, Material: KS-HF (KDM)
Transformer T_1 and T_2	Turns ratio: $n_1/n_2/n_3 = 12:12:1$ Magnetizing inductor $L_{\text{M}1}$ and $L_{\text{M}2}$: 25μH BUS: 12 turns, litz wire 0.1mm×400 strands (1.7mΩ) HV: 12 turns, litz wire 0.1mm×400 strands (1.7mΩ) LV: 1 turn, copper wire 0.2mm×12.5mm×10 (0.1mΩ) Form: BUS and HV in series, LV in parallel Core: PQ50/50, Material: 3C95 (DMEGC) Leakage inductance of port1,2,3: 0.5μH, 0.5μH, 30nH
BUS port Π filter	HF caps.C_{11}: 4*5μF/500Vdc in parallel (Faratronic) LF caps.C_{12}: 3*470μF/450Vdc (KNSCHA) HF ind.$L_{\text{r}1}$: 0.47μH/30A (cjiang)
HV port Π filter	HF caps.C_{21} and C_{22}: 1*5μF/500Vdc (Faratronic) HF ind.$L_{\text{r}2}$: 0.47μH/30A (cjiang)
LV port Π filter	HF caps.C_{31}: 20*47uF/25Vdc in parallel (muRata) LF caps.C_{32}: 4*2200μF/25Vdc in parallel (Rubycon) HF ind.$L_{\text{r}3}$: 100nH/25A in parallel (cjiang)

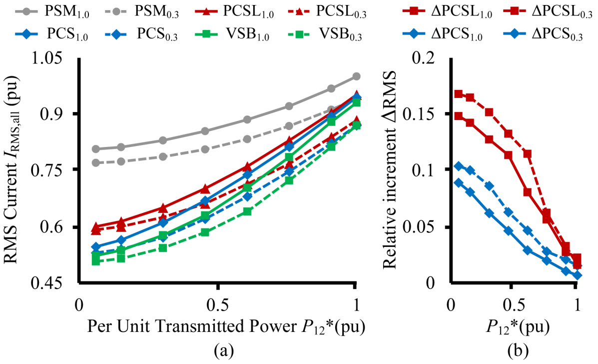

(a) (b)

Fig. 14. Control diagram of the proposed control scheme.

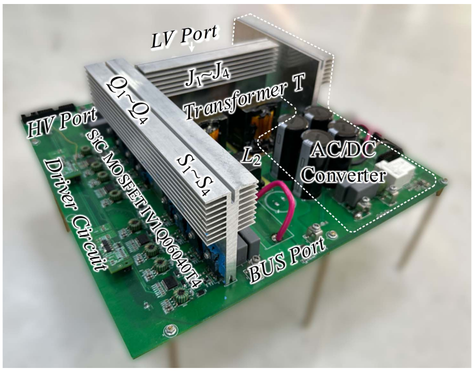

Fig. 15. Photograph of the DTAB test platform.

As can be seen, in the CV charging mode, the VSB and PSM schemes, without ZVS compensation measures, achieve the six-ZVS operation (i.e., all-ZVS operation) only in the middle load and above, while, in the CP charging mode, only two-ZVS operation is achieved in most voltage ranges. In the PCS scheme, ZVS operation is achieved in the slave ports' switches through the phase-shift compensation. Therefore, there are at least four bridge arms that perform ZVS operation in both CV and CP charging modes. In the PCSL scheme, the well-tuned magnetizing inductance design enables ZVS operation in the master port's switches, allowing all-ZVS operation achieved under any operating condition. Consequently, the PCSL scheme exhibits the widest characteristic of the ZVS range, enabling the DTAB system to achieve all-ZVS operation across the entire voltage and power range.

C. Inductor Rms Current Comparisons

Although the introduction of phase-shift compensation and magnetizing inductance proves beneficial for expanding the ZVS range, it is inevitable that additional back-flow power would be introduced by both measures, leading to a potential increase in the rms current of the system. Consequently, it is essential to compare the rms current characteristic of the aforementioned schemes, as this current is closely tied to the conduction losses of the system.

Fig. 14(a) illustrates the comparison of rms currents for the four schemes under $V_1 = 396$ V, $V_2' = 336$ V, $V_3' = 12$ V, $P_2^* = [0-1]$ condition, with the subscript "x" in the legend denoting the unified value of power P_3, i.e., $P_3^* = x$. As observed, the VSB scheme exhibits optimal rms current characteristics throughout all power ranges, while the PSM scheme performs the worst. In both PCS and PCSL schemes, both rms currents are larger than that of the VSB scheme, but remain superior to the PSM scheme.

Fig. 14(b) presents the relative increment ΔRMS of PCSL and PCS schemes compared to the VSB scheme. Evidently, for most power ranges, ΔRMS of the PCS scheme remains within 10%, particularly staying below 5% when $P_{12}^* > 0.5$. With the injection of magnetizing current in the PCSL scheme, ΔRMS is larger than that of the PCS scheme. Although the maximum increment of PCSL occurs at light-load conditions, the value of the rms current is relatively small and the switching loss dominates the overall loss. Furthermore, although the conduction loss plays the dominant role of the overall loss under the heavy load condition, ΔRMS of the PCSL scheme gradually decreases with transmitted power and stays below 10% when $P_{12}^* > 0.5$, thus the effect of the magnetizing current on the efficiency of the system can be reduced.

VI. EXPERIMENTAL VERIFICATION

To validate the theoretical analysis presented in this study, a DTAB converter tailored for EVs' charging system performed at 3.3 kW/100 kHz condition is shown in Fig. 15, whose detailed parameters are listed in Table IV. Notably, port 1 is cascaded with a single-stage ac/dc converter, and ports 2 and 3 are, respectively, connected to a high-voltage power battery and low-voltage auxiliary battery. To reduce the number of turns ratio and improve the heat dissipation capability, the three-port transformer is divided into two parts connected in series on the V_1 and V_2' side (high-voltage side) and in parallel on the V_3' side (low-voltage side). In addition, the design of inductance values in this system is relatively small [taking 0.3 times $L_{\text{i,jmax}}$ and $L_{\text{i,jmax}} = V_{\text{i}}V_{\text{j}}/(8f_{\text{s}}P_{\text{ij,max}})$], which enables the system to operate with relatively small phase-shift angles under rated conditions, thus offering a superior rms current characteristic. It should be noted that the magnetizing inductance L_{M} is integrated into each transformer, and each value converted to the V_1 side is 25 μH, determined by (15).

A. Steady State Verifications

For experimental benchmarking, the following schemes capable of on-line close-loop control are selected: the PCSL scheme (including phase-shift compensation and well-tuned magnetizing inductance), the VSB scheme (volt–sec balanced control in [23] and [26]) and the PSM scheme in Michon et al.'s [19] work (corresponds to the SPS control in DAB converters).

1) Light Load Verification: The steady state operation waveforms of the three control schemes under the light load condition are illustrated in Fig. 16. Here, $V_3 < V_2 < V_1$ and both slave ports operate under the buck condition. As observed, in the PSM scheme, the ZVS operation is only achieved in the master port since the phase-shift angles in the PSM scheme are limited to

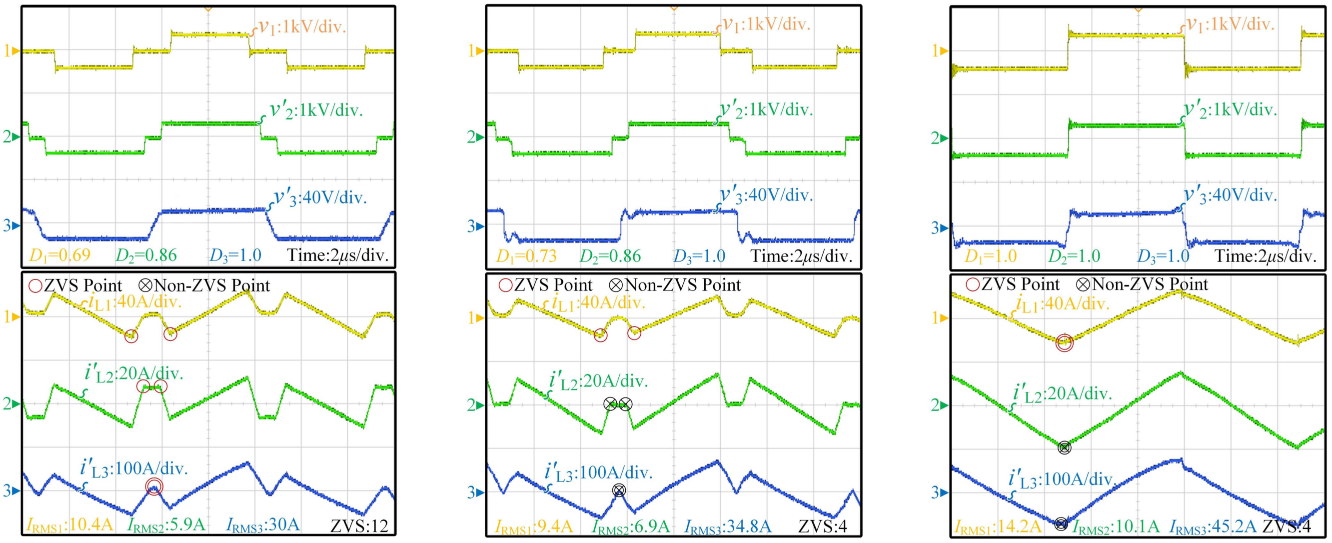

(a) (b) (c)

Fig. 16. Typical operation waveforms at $V_1 = 396$ V, $V'_2 = 336$ V, $V'_3 = 12$ V, $P_2 = 500$W, $P_3 = 300$W. (a) PCSL. (b) VSB. (c) PSM.

1, lacking the capability of optimizing the ZVS range. Furthermore, the PSM scheme exhibits the highest peak current and rms current characteristics. In the VSB scheme, the phase-shift angles are regulated by the volt–sec balance principle, offering a lower rms current compared to PSM scheme. In the PCSL scheme, the D_1 is further reduced to guarantee ZVS operations of two slave ports' switches. Although the influence of the magnetizing inductance is considered in the PCSL scheme, the increment of RMS current is relatively small compared to VSB scheme.

2) ZVS Operation Verification: Fig. 17 provides a detailed comparison of the ZVS operating states between the PCSL and VSB schemes under light load condition. As observed, all-ZVS operation has been achieved in the PCSL scheme. In contrast, for the ZCS-operating switches in the VSB scheme, the energy stored in the switch's body capacitance cannot be released in advance. This results in an overlap in $v_{\rm ds}$ and $v_{\rm gs}$ at zero current, where the energy of body capacitance in this region can only be dissipated as heat loss, causing a decrease in efficiency and the appearance of voltage spikes.

3) Heavy Load Verification: Fig. 18 depicts the waveforms of the three control schemes under heavy load condition, operated at the maximum high-voltage battery voltage $V'_2 = 450$V. Herein, the voltage sequence is $V_2 > V_1 > V_3$, resulting in the minimum phase-shift angle D_2 for Port 2. It is evident that the PCSL scheme maintains all-ZVS operation, whereas the ZVS operation in the VSB scheme is only achieved in six switches. In the PSM scheme, ZVS operation fails in port 1 and 3, resulting in noticeable voltage spikes in v_1 and v'_3. Furthermore, the PSM scheme still exhibits the highest rms current. With the increase of output power, the rms currents in the PCSL scheme and the VSB scheme are comparable, since the additional magnetizing current is relatively small in comparison to the inductance current for power transmission.

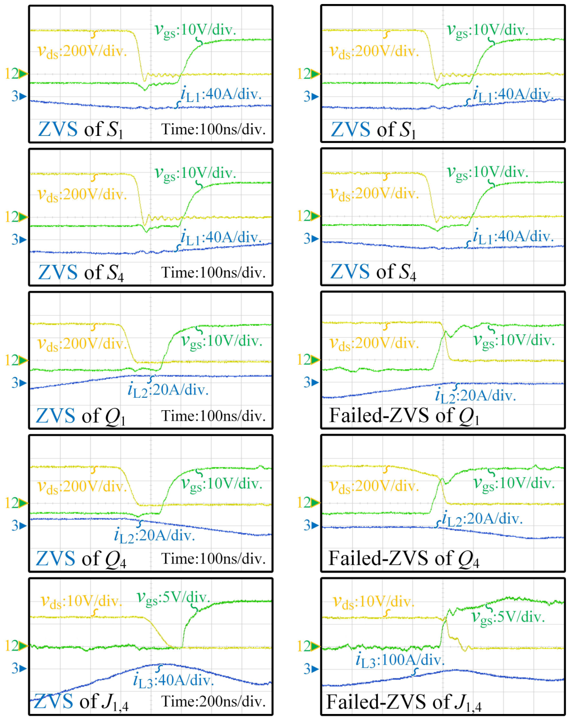

(a) (b)

Fig. 17. ZVS states of all switches in PCSL and VSB at $V_1 = 396$ V, $V'_2 = 336$ V, $V'_3 = 12$ V, $P_2 = 500$W, $P_3 = 300$W. (a) Waveforms in the PCSL scheme. (b) Waveforms in the VSB scheme.

B. Dynamic Operation Verifications

1) CV Charging Mode Verification: Fig. 19 illustrates the dynamic waveforms of the PCSL scheme operating in CV charing mode. The power ranges of ports 2 and 3 are specified as

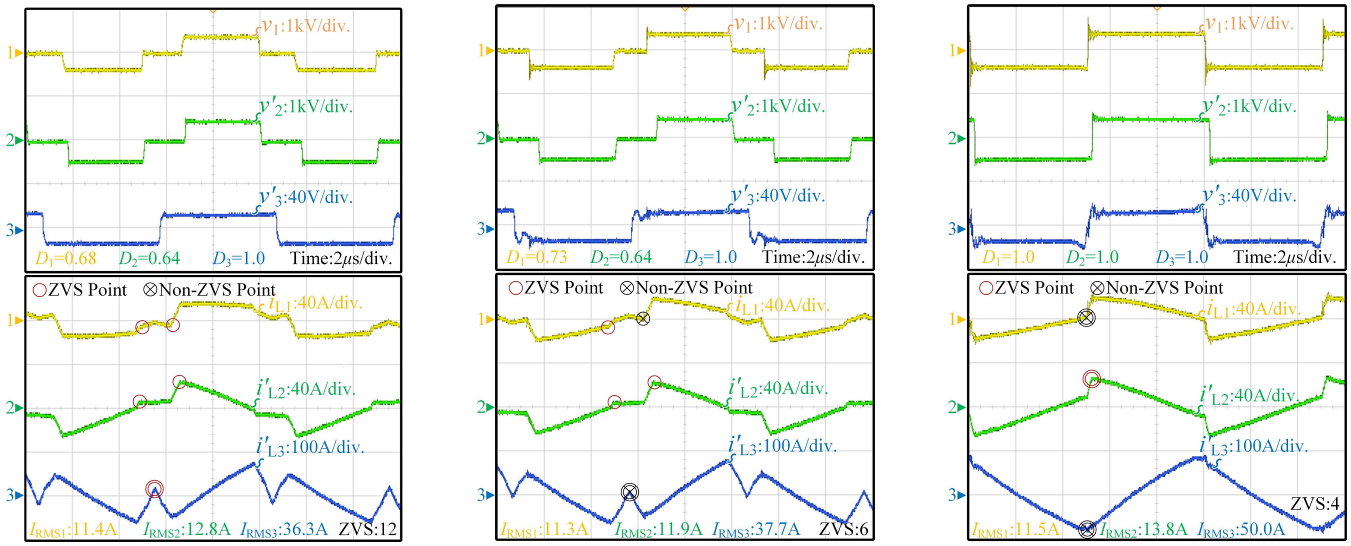

(a) (b) (c)

Fig. 18. Typical operation waveforms at $V_1 = 396$ V, $V_2' = 450$ V, $V_3' = 12$ V, $P_2 = 3.3$kW, $P_3 = 300$W. (a) PCSL. (b) VSB. (c) PSM.

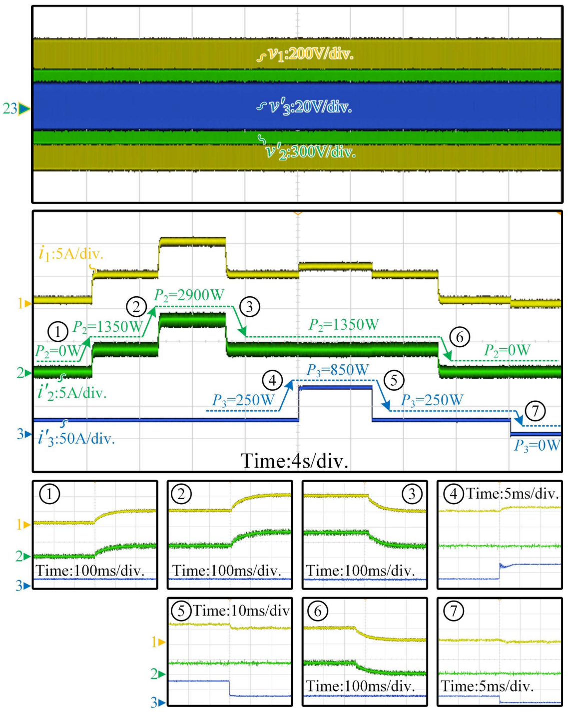

Fig. 19. Dynamic responses of the PCSL in CV mode at $V_1 = 396$ V, $V_2' = 336$ V, and $V_3' = 12$ V.

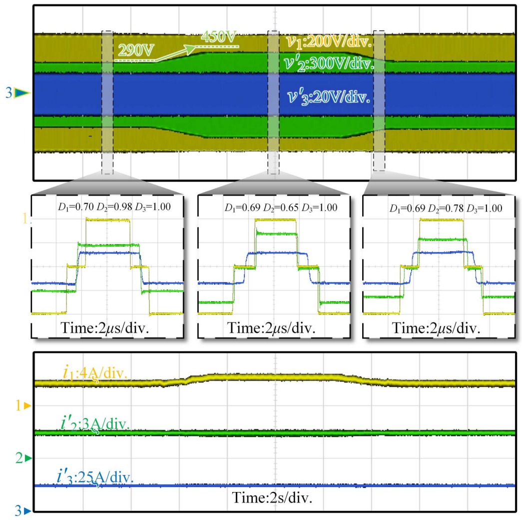

Fig. 20. Dynamic responses of the PCSL in CC mode at $I_2' = 3$A, $I_3' = 25$A with $V_1 = 396$ V, $V_2' = [290\,\text{V}, 450\,\text{V}]$, $V_3' = 12$ V.

$P_2 = (0, 1350, 2900)$W and $P_3 = (0, 250, 850)$W, respectively. Due to the large capacity nature of the high-voltage battery in port 2, the charging process of the battery is inherently slow, and its dynamic response time is typically required to be on the order of 100 ms. On the contrary, port 3 is linked to a smaller capacity low-voltage battery, where noticeable voltage fluctuations would occur with changes in on-board loads. Consequently, a strong dynamic response capability is required in port 2, with a dynamic response time typically on the order of 1 ms. As observed, the stable operation of the PCSL scheme is also achieved during load transients, and the performances of dynamic responses satisfy the demands of two batteries. It is worth noting that during power transients in port 2 or 3, the output current of the other port remains constant without coupling fluctuations, confirming the excellent power decoupling characteristics of the DTAB converter.

2) CC Charging Mode Verification: Fig. 20 showcases the dynamic waveforms of the PCSL scheme operating at the CC charging mode. Here, the output currents are configured to $I_2' = 3$A, $I_3' = 25$A, and a voltage-source-type power supply is employed to simulate the charging process of the high-voltage battery, increasing from a voltage of 290 to 450 V. As can be

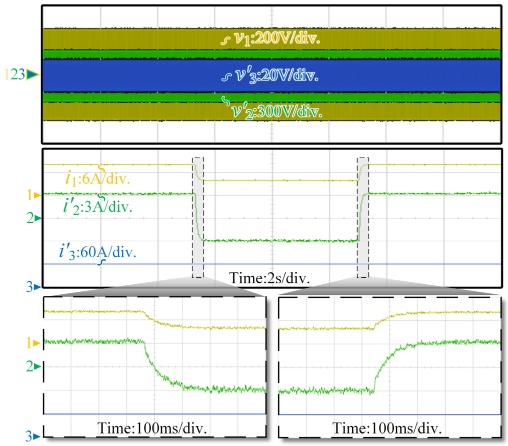

Fig. 21. Bidirectional operation of the PCSL in CV mode at $V_1 = 396\,\text{V}$, $V_2' = 336\,\text{V}$, $V_3' = 12\,\text{V}$ with $I_2' = [-3, 3]\text{A}$, $I_3' = 60\text{A}$.

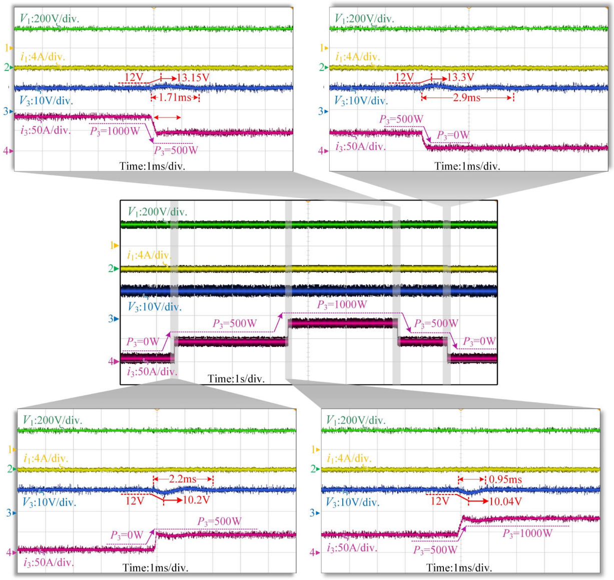

Fig. 22. Dynamic waveforms of DTAB converters under $V_1 = 396\,\text{V}$, $V_2' = 336\,\text{V}$, $V_3' = 12\,\text{V}$ with $P_1 = -750\text{W}$, $P_3 = [0, 1]\text{kW}$.

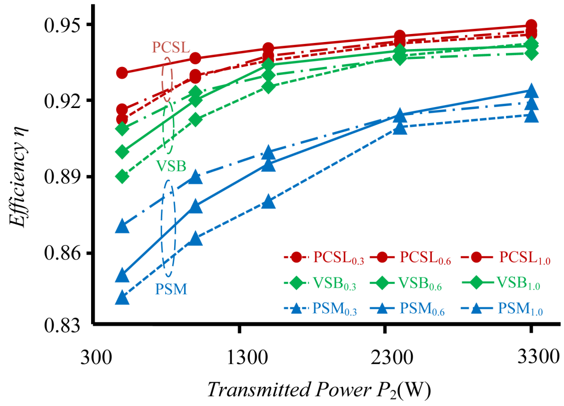

Fig. 23. Efficiency comparisons in CV mode at $V_1 = 396\,\text{V}$, $V_2' = 336\,\text{V}$, $V_3' = 12\,\text{V}$.

seen, the charging process is smoothly executed in the entire voltage range, with the phase-shift D_2 decreased from 0.98 to 0.65. Therefore, by combining with the PCSL scheme, stable operation can still be achieved in the CC charging mode.

3) Bidirectional Charging Mode Verification: Fig. 21 depicts the dynamic waveforms of the PCSL scheme operating at the bidirectional charging mode, where the output current of port 2 is set to $I_2' = [-3, 3]\text{A}$. For $I_2' = -3\text{A}$, both port 1 and port 2 function as inputs and port 3 serves as the output. When $I_2' = 3\text{A}$, only port 1 operates as the input, while both port 2 and 3 serve as outputs. Benefiting from the straightforward control characteristic of the PCSL scheme, the bidirectional charging operation can be readily realized by regulating the value of Φ_{12}. Furthermore, the transient process can be smoothly achieved, eliminating the need for intricate switching designs found in conventional PSM schemes.

4) V2G+Dc/Dc Mode Verification: To demonstrate the voltage regulation capability of proposed control strategy clearly under load variations, it is feasible to operate the DTAB converter in vehicle to grid (V2G) + dc/dc mode, where the whole system acquires energy from the HV port and transfers power to the BUS and LV ports. As shown in Fig. 22, the power range of port 3 is specified as [0, 1kW], it is evident that the rapid and stable close-loop control can be achieved during LV port's load variations. In each subplot, dynamic regulations of V_3 can be realized within the millisecond range, with voltage overshoots maintained at around 15%. Benefiting from the decoupling characteristics of the DTAB converter, no coupling issues in V_1 or i_1 are observed at the BUS port.

In summary, the dynamic operations of the PCSL scheme under the CC, CV, bidirectional charging and V2G+dc/dc modes are thoroughly examined. Experimental results demonstrate that the PCSL scheme is capable of achieving stable operation of the DTAB converter during transient processes.

C. Efficiency and Power Loss Comparison

1) Comparison Under the Entire Power Range: Fig. 23 provides the efficiency comparisons of the PCSL scheme, VSB scheme and PSM scheme under the CV mode across the entire power range, where the subscript "x" in the legend denotes the unified value of power P_3, i.e., $P_3^* = x$. As observed, due to the limitations of ZVS operation and rms current, the operational efficiency in the PSM scheme is the lowest across the entire power range. In contrast, by maintaining VSB principle, superior conduction and switching losses can be achieved in the VSB scheme, achieving higher operational efficiencies than the PSM scheme. Compared to the VSB scheme, the ZVS range of DTAB converters can be further extended by the PCSL scheme, providing a maximum efficiency improvement of 3% under light load conditions and reaching a peak efficiency of 95% across the entire power range. With the power P_2 increases, the operational efficiency of the VSB and PCSL schemes gradually converges, but the efficiency of the PCSL scheme still prevails over that of the VSB scheme.

2) Comparison Under the Entire Voltage Range: Fig. 24 illustrates the the efficiency comparisons of the three schemes

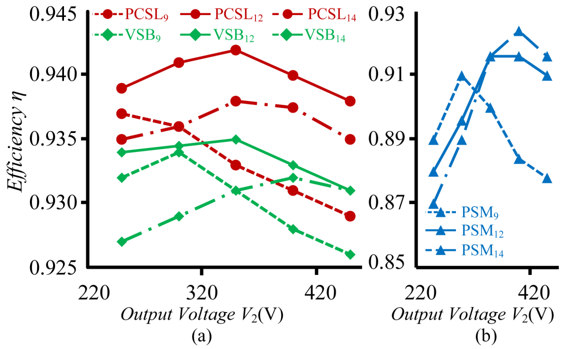

Fig. 24. Efficiency comparisons in CP mode at $V_1 = 396\,\text{V}$, $V_2' = [250\,\text{V}, 450\,\text{V}]$, $V_3' = [9\,\text{V}, 14\,\text{V}]$, $P_2' = 1500\text{W}$, $P_3' = 600\text{W}$. (a) Results of the PCSL and VSB schemes. (b) Results of the PSM scheme.

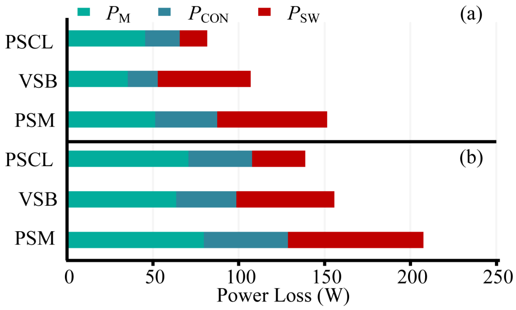

Fig. 25. Loss comparison results. (a) Result at $V_1 = 396\,\text{V}$, $V_2' = 336\,\text{V}$, $V_3' = 12\,\text{V}$, $P_2 = 500\text{W}$, $P_3 = 300\text{W}$. (b) Result at $V_1 = 396\,\text{V}$, $V_2' = 450\,\text{V}$, $V_3' = 12\,\text{V}$, $P_2 = 1500\text{W}$, $P_3 = 600\text{W}$.

under the CP mode across the entire voltage range, where the subscript "x" in the legend denotes the voltage of V_3', i.e., $V_3' = x\,\text{V}$. As can be seen, the PCSL scheme consistently maintains the highest operational efficiency across the entire voltage range. Moreover, this efficiency advantage becomes more pronounced under a higher V_2 condition, since the switching-ON loss in VSB or PSM scheme cannot be fully eliminated, and this loss is positively correlated with switches' drain-to-source voltage. In addition, similar to the characteristic observed in DAB converters that operational efficiency peaks at the voltage-match point, the efficiency curves of all three schemes exhibit a wave trend across the entire voltage range.

3) Loss Comparison: Fig. 25 showcases a power loss breakdown for the three control schemes. Generally, the major loss of the system can be divided into the magnetizing loss P_{M}, the conduction loss P_{CON}, and the switching loss P_{SW} [29], [30]. The operating condition of Fig. 25(a) corresponds to the aforementioned steady-state experiment under light load condition. According to Fig. 16(c), the PSM scheme exhibits the highest rms current characteristic, resulting in an elevated magnetizing loss P_{M} and conduction loss P_{CON}. As the influence of magnetizing inductance is introduced in the PCSL scheme, compared to those in the VSB scheme, higher P_{M} and P_{CON} are observed due to the extra injection of magnetizing current. However, benefiting from the achievement all-ZVS operation, the switching loss of the PCSL scheme is significantly reduced, allowing for a lowest power loss performance among the three control schemes.

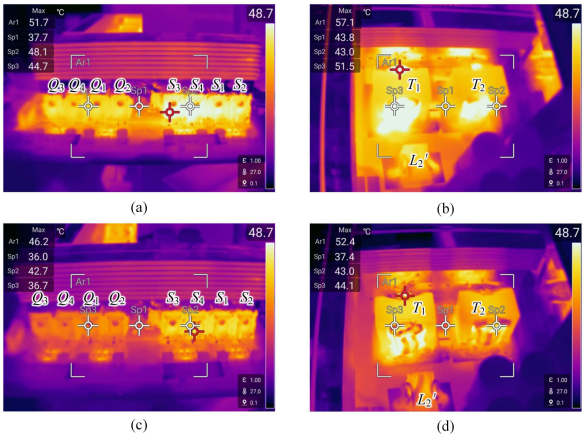

Fig. 26. Thermal images under $V_1 = 396\,\text{V}$, $V_2' = 336\,\text{V}$, $V_3' = 12\,\text{V}$, $P_2 = 3300\text{W}$, $P_3 = 300\text{W}$ condition. (a) Magnetic components under PSM scheme. (b) High-voltage switches under PSM scheme. (c) Magnetic components under PCSL scheme. (d) High-voltage switches under PCSL scheme.

The operating condition of Fig. 25(b) corresponds to the aforementioned steady-state experiment under heavy load conditions. With the increase of transmitted power, the magnetizing current becomes relatively small compared to the inductance current for power transmission. Therefore, the magnetizing loss P_{M} and the conduction loss P_{CON} in the PCSL scheme are close to the VSB scheme. As transmitted power increases, the switching loss in the PCSL scheme increases, but remains the minimum among all control schemes.

4) Temperature Comparison: To visually demonstrate the advantages of proposed control scheme, a series of thermal images of the converter operating at a full load are shown in Fig. 26(a) and 26(b) depict the thermal images obtained through the PSM scheme, where the ZVS operation of switches $S_1 - S_4$ cannot be achieved, resulting in the increment of switching losses, with the maximum temperature of $S_1 - S_4$ reaching 47.7 °C. And the transformer's maximum temperature reaches 54.1 °C. Conversely, Fig. 26(c) and (d) presents the thermal images obtained with the PCSL scheme. Under the proposed control law, the rms current and current stress in three ports can be reduced, and ZVS operation can be achieved in all switches. Therefore, the magnetic loss, conducting loss, switching loss can be simultaneously optimized, leading to the maximum temperature of $S_1 - S_4$ and transformer decreasing to 52.4 °C and 46.2 °C, respectively.

To sum up, the PSM scheme performances the worst operational efficiency due to the low phase-shift dimension. Although the concept of magnetizing inductance design [26] is introduced in TAB converters, the equivalent circuit of DTAB converters changes, leading to an increased switching-on loss compared to the PCSL scheme. Therefore, the PCSL scheme owns the highest efficiency for the DTAB converters.

VII. CONCLUSION

In this article, a hybrid software–hardware all-ZVS operation strategy is proposed to enhance the operational efficiency of the high-frequency DTAB converter. First, the power decoupling characteristic of the DTAB converter are analyzed and the challenges of expanding the ZVS range with the widely adopted VSB control are highlighted. Subsequently, to broaden the ZVS range of DTAB converters, a unified ZVS model is established based on the complete circuit response equation. This model simplifies the derivation of ZVS conditions and is universally applicable to TAB converters as well. Building upon the unified model, the ZVS condition of the VSB control is derived, and a simplified QPS modulation scheme is proposed to facilitate the realization of ZVS operation for the switches in the slave ports. Furthermore, the influence of the magnetizing inductance in DTAB converters is considered in this article, noting its beneficial role in achieving ZVS operation due to its inductive current. The optimal design customized for DTAB converters is also proposed, by which the ZVS operation of switches in the master port can be achieved. Notably, all above-mentioned analysis is derived from the DAB converter based on the time domain, enabling this hybrid strategy to be computationally stress-free and easily replicable, particularly advantageous for EVs charging system.

Finally, a customized 3.3 kW/100 kHz DTAB prototype for EVs charging system was constructed. Comprehensive steady-state and dynamic operation experiments thoroughly demonstrated the effectiveness of the proposed control scheme. Efficiency and loss analysis indicate that the PCSL scheme features superior efficiency characteristics over conventional control schemes, with a maximum efficiency improvement of 3% under light load conditions and a peak efficiency of 95% throughout the power range.

REFERENCES

[1] A. K. Bhattacharjee, N. Kutkut, and I. Batarseh, “Review of multiport converters for solar and energy storage integration,” *IEEE Trans. Power Electron.*, vol. 34, no. 2, pp. 1431–1445, Feb. 2019.

[2] J. Xu et al., “Automatic time-division multiplexing for inductive power transfer to multiple stainless-steel-enclosed receivers,” *IEEE Trans. Emerg. Sel. Topics Power Electron.*, vol. 12, no. 2, pp. 2333–2344, Apr. 2024.

[3] L. Jiang et al., “A variable tertiary DC-link voltage control for integrated APM in EV charger systems featuring full ZVS range,” *IEEE Trans. Transp. Electrific.*, early access, Jan. 12, 2024, doi: 10.1109/TTE.2024.3353490.

[4] H. Chen, Z. Hu, H. Luo, J. Qin, R. Rajagopal, and H. Zhang, “Design and planning of a multiple-charger multiple-port charging system for PEV charging station,” *IEEE Trans. Smart Grid*, vol. 10, no. 1, pp. 173–183, Jan. 2019.

[5] J. Schäfer, D. Bortis, and J. W. Kolar, “Multi-port multi-cell DC/DC converter topology for electric vehicle’s power distribution networks,” in *Proc. 2017 IEEE 18th Workshop Control Model. Power Electron. (COMPEL)*, 2017, pp. 1–9.

[6] I. Biswas, D. Kastha, and P. Bajpai, “Small signal modeling and decoupled controller design for a triple active bridge multiport DC–DC converter,” *IEEE Trans. Power Electron.*, vol. 36, no. 2, pp. 1856–1869, Feb. 2021.

[7] L. Wang, Z. Wang, and H. Li, “Asymmetrical duty cycle control and decoupled power flow design of a three-port bidirectional DC-DC converter for fuel cell vehicle application,” *IEEE Trans. Power Electron.*, vol. 27, no. 2, pp. 891–904, Feb. 2012.

[8] J. Chen, L. Gong, W. Li, J. Cai, and Y. Wang, “Simplified power decoupling control of triple active bridge converter in polar coordinate system for EV application,” *IEEE Trans. Ind. Electron.*, early access, Mar. 21, 2024, doi: 10.1109/TIE.2024.3370979.

[9] P. Wang, S. Zhang, D. Xu, and X. Lu, “A series-resonance-based three-port converter with unified autonomous control method in DC microgrids,” in *Proc. 2018 IEEE Appl. Power Electron. Conf. Expo. (APEC)*, 2018, pp. 3270–3274.

[10] J. Wu, X. Yan, X. Sun, X. Su, H. Du, and X. Wang, “A series resonant three-port DC–DC converter with decoupling function and magnetic integration,” *IEEE Trans. Power Electron.*, vol. 37, no. 12, pp. 14720–14737, Dec. 2022.

[11] K. Wang, W. Liu, and F. Wu, “Topology-level power decoupling three-port isolated current-fed resonant DC-DC converter,” *IEEE Trans. Ind. Electron.*, vol. 69, no. 5, pp. 4859–4868, May 2022.

[12] Y. Wang, F. Han, L. Yang, R. Xu, and R. Liu, “A three-port bidirectional multi-element resonant converter with decoupled power flow management for hybrid energy storage systems,” *IEEE Access*, vol. 6, pp. 61331–61341, 2018.

[13] S. Hazra, S. Bhattacharya, and C. Chakraborty, “A novel control principle for a high frequency transformer based multiport converter for integration of renewable energy sources,” in *Proc. IECON 2013-39th Annu. Conf. IEEE Ind. Electron. Soc.*, 2013, pp. 7984–7989.

[14] S. Bandyopadhyay, P. Purgat, Z. Qin, and P. Bauer, “A multiactive bridge converter with inherently decoupled power flows,” *IEEE Trans. Power Electron.*, vol. 36, no. 2, pp. 2231–2245, Feb. 2021.

[15] D.-U. Kim, B. Byen, B. Jeong, and S. Kim, “Design of triple-active bridge converter with inherently decoupled power flows,” in *Proc. 2022 24th Eur. Conf. Power Electron. Appl. (EPE’22 ECCE Europe)*, 2022, pp. 1–9.

[16] P. Purgat, S. Bandyopadhyay, Z. Qin, and P. Bauer, “Zero voltage switching criteria of triple active bridge converter,” *IEEE Trans. Power Electron.*, vol. 36, no. 5, pp. 5425–5439, May 2021.

[17] S. Dey, A. Mallik, and A. Akturk, “Investigation of ZVS criteria and optimization of switching loss in a triple active bridge converter using penta-phase-shift modulation,” *IEEE Trans. Emerg. Sel. Topics Power Electron.*, vol. 10, no. 6, pp. 7014–7028, Dec. 2022.

[18] J. Li, Q. Luo, T. Luo, D. Mou, and M. Liserre, “Efficiency optimization scheme for isolated triple active bridge DC–DC converter with full soft-switching and minimized RMS current,” *IEEE Trans. Power Electron.*, vol. 37, no. 8, pp. 9114–9128, Aug. 2022.

[19] M. Michon, J. Duarte, M. Hendrix, and M. Simoes, “A three-port bi-directional converter for hybrid fuel cell systems,” in *Proc. 2004 IEEE 35th Annu. Power Electron. Specialists Conf. (IEEE Cat. No.04CH37551)*, 2004, pp. 4736–4742, vol. 6.

[20] G. Xu, D. Sha, Y. Xu, and X. Liao, “Hybrid-bridge-based DAB converter with voltage match control for wide voltage conversion gain application,” *IEEE Trans. Power Electron.*, vol. 33, no. 2, pp. 1378–1388, Feb. 2018.

[21] G. Xu, L. Li, X. Chen, W. Xiong, X. Liang, and M. Su, “Decoupled EPS control utilizing magnetizing current to achieve full load range ZVS for dual active bridge converters,” *IEEE Trans. Ind. Electron.*, vol. 69, no. 5, pp. 4801–4813, May 2022.

[22] A. K. Jain and R. Ayyanar, “PWM control of dual active bridge: Comprehensive analysis and experimental verification,” *IEEE Trans. Power Electron.*, vol. 26, no. 4, pp. 1215–1227, Apr. 2011.

[23] H. Tao, A. Kotsopoulos, J. L. Duarte, and M. A. M. Hendrix, “Transformer-coupled multiport ZVS bidirectional DC–DC converter with wide input range,” *IEEE Trans. Power Electron.*, vol. 23, no. 2, pp. 771–781, Mar. 2008.

[24] H. Wang et al., “Universal phase-shift modulation scheme and efficiency optimization for modular multiactive bridge converter,” *IEEE Trans. Ind. Electron.*, vol. 71, no. 7, pp. 7312–7321, Jul. 2024.

[25] J. Riedel, D. G. Holmes, B. P. McGrath, and C. Teixeira, “Maintaining continuous ZVS operation of a dual active bridge by reduced coupling transformers,” *IEEE Trans. Ind. Electron.*, vol. 65, no. 12, pp. 9438–9448, Dec. 2018.

[26] L. Gong et al., “A simplified ALL-ZVS strategy for high-frequency triple active bridge converters with designed magnetizing inductance,” *IEEE Trans. Power Electron.*, vol. 38, no. 11, pp. 13781–13797, Nov. 2023.

[27] S. Dey and A. Mallik, “Multivariable-modulation-based conduction loss minimization in a triple-active-bridge converter,” *IEEE Trans. Power Electron.*, vol. 37, no. 6, pp. 6599–6612, Jun. 2022.

[28] L. Gong et al., “A dynamic ZVS-guaranteed and seamless-mode-transition modulation scheme for the DAB converter that maximizes the ZVS range and lowers the inductor RMS current,” *IEEE Trans. Power Electron.*, vol. 37, no. 11, pp. 13119–13134, Nov. 2022.

[29] Y. Tang et al., “Reinforcement learning based efficiency optimization scheme for the DAB DC–DC converter with triple-phase-shift modulation,” *IEEE Trans. Ind. Electron.*, vol. 68, no. 8, pp. 7350–7361, Aug. 2021.

[30] J. Chen, J. Xu, Y. Zhang, J. Zhao, J. Hou, and Y. Wang, “Geometrical state-plane-based synchronous rectification scheme for LLC converter in EVs,” *IEEE Trans. Transp. Electrific.*, early access, Apr. 1, 2024, doi: 10.1109/TTE.2024.3383208.

Linxiao Gong (Graduate Student Member, IEEE) was born in Guang'an, China, in 1998. He received the B.S. degree in electrical engineering from Southwest JiaoTong University, Sichuan, China, in 2020. He is currently working toward the Ph.D. degree in electrical engineering with Shanghai Jiao Tong University, Shanghai, China.

His current research interests include advanced control and modulation for dc–dc converters and multiport power converters.

Yunfeng Peng received Ph.D. degree in management science and engineering from Shanghai Jiaotong University, Shanghai, China, in 2016.

He has the system engineering education background of cross-integration of high-end equipment, information technology and management science, and the collaborative innovation practice experience of government, industry and academia. In 2020, he joined joined the School of Electronic Information and Electrical Engineering, Shanghai Jiao Tong University, and was a dual hired Teacher with Antai School of Economics and Management, Shanghai, creating the International Intelligent Innovation Design Research Center. His research interests include new energy system engineering and innovation and entrepreneurship management.

Junzhong Xu (Member, IEEE) was born in Ningbo, China, in 1994. He received the B.S. degree in electrical engineering from the Harbin Institute of Technology, Harbin, China, in 2016, and the Ph.D. degree in electrical engineering from Shanghai Jiao Tong University, Shanghai, China, in 2021.

From 2020 to 2021, he was a Visiting Scholar with the DC Systems, Energy Conversion and Storage Group, Delft University of Technology, Delft, The Netherlands. He was a Postdoctoral Research Fellow with the Department of Electrical Engineering, Shanghai Jiao Tong University, in 2021. He is currently with Power Electronic Systems (PES) Laboratory, the Swiss Federal Institute of Technology (ETH), Zurich, Switzerland. His research focuses on advanced control and modulation for power converters.

Dr. Xu was the recipient of Outstanding PhD Thesis Award from Shanghai Jiao Tong University in 2021.

Wenhui Li was born in Lishui, China, in 2000. He received the B.S. degree in electrical engineering in 2022 from Shanghai Jiao Tong University, Shanghai, China, where he is currently working toward the M.S. degree in electrical engineering.

His research interests include optimal control for dc/dc converters and modeling of multiport converters.

Xing Fang (Student Member, IEEE) was born in Huangshan, China, in 2001. She received the B.S. degree in electrical engineering from Chongqing University, Chongqing, China, in 2023. She is currently working toward the Ph.D. degree in electrical engineering with Shanghai Jiao Tong University, Shanghai, China.

Her current research focuses on the control and modulation strategy in ac–dc converters.

Jian Wang received the B.S. degree in electrical engineering from North China Electric Power University, Beijing, China, in 2018, and the joint Ph.D. degree in electrical engineering from Shanghai Jiao Tong University, Shanghai, China, and Politecnico di Milano, Milan, Italy, in 2023.

She joined Shanghai Jiao Tong University in 2023 as an Assistant Research Fellow with the College of Smart Energy. Her research interests include dc–dc converter, optimal operation of virtual power plant, and integrated energy systems.

Yong Wang (Member, IEEE) received Ph.D. degree in power electronics from Zhejiang university, Hangzhou, China, in 2005.

From 2005 to 2008, he was a Senior Researcher with Samsung Advanced Institute of Technology, Yongin, South Korea, working on the fuel cell grid tied inverter. From 2008 to 2010, he was with Danfoss Solar Inverters, Soenderborg, Denmark, as a power electronics Hardware Engineer. In 2010, he joined Shanghai Jiao Tong University, Shanghai, China, where he is currently a Full Professor with the Department of Electrical Engineering. His research interests include new energy storage system and electric vehicle power supply systems.